Effect of Boundary Misorientation on Yielding Behavior of Nanostructured High Purity Aluminium

To understand deformation mechanisms of nanostructured metals, effect of boundary misorientation on yielding behavior of nanostructured aluminium has been investigated. It has been suggested that in the grain size less than 10 μm an extra hardening mechanism due to lack of dislocation sources is responsible for the high strength, and that high-angle boundaries are more effective for strengthening than low-angle boundaries.

Introduction

Nanostructured metals produced by high strain deformation, with an average grain size less than 1 μm, are found to show several unique mechanical properties, such as unexpected yield point phenomena in pure aluminium, extra Hall-Petch hardening, annealing-induced hardening and deformation-induced softening [1-4]. However, detailed deformation mechanisms of nanostructured metals have not yet been understood. Since nanostructured metals are characterized by a high density of grain boundaries, interaction between dislocations and grain boundaries is expected to be much significant in nanostructured metals, and such effect may strongly depend on the boundary misorientation. In the present work, the effect of boundary misorientation on yielding behavior of nanostructured aluminium has been investigated.

Experimental

A fully-recrystallized high purity aluminium was deformed by conventional rolling to 50% reduction at room temperature, followed by annealing treatment to obtain subgrained structures composed of low-angle boundaries. In the annealing treatment, two-step annealing process [5] was used to change the structural size without discontinuous recrystallization. To produce ultrafine grained samples mainly surrounded by high-angle boundaries, high strain deformation followed by two-step annealing was used, where accumulative roll-bonding (ARB) of 6 cycles was applied to give a high strain [3,6].

Microstructures of the obtained samples were characterized by electron backscatter diffraction (EBSD) and transmission electron microscopy (TEM). Mechanical properties were determined by tensile test at room temperature, where an initial strain rate is 8.3 x 10^{-4} s^{-1}.

Results and Discussion

The 50% rolled sample showed a typical dislocation cell structure, containing dislocation cell boundaries and individual dislocations between the boundaries. By annealing at 175°C for 24 h, recovery mainly occurred and the dislocation cell structure was changed into a typical subgrained structure with the average subgrain size of 0.88 μm (Fig. 1a). Additional high-temperature annealing led to a slight subgrain coarsening. The EBSD measurements have proved that boundaries in these subgrained structures are mainly low-angle boundaries with misorientation angle less than 15°. Such samples mainly surrounded by low-angle boundaries are hereafter referred to as "subgrained" samples.

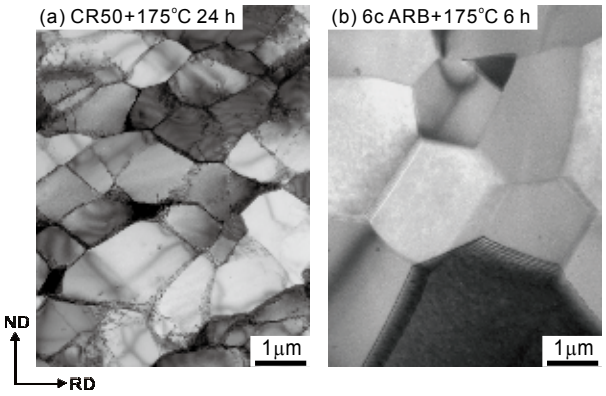

Fig. 1 TEM microstructures of the deformed and annealed samples. (a) 50% rolled and annealed at 175°C for 24 h, (b) 6-cycle ARB processed and annealed at 175°C for 6 h.

After ARB of 6 cycles, on the other hand, ultrafine grained structure with an average grain size of 0.69 μm was obtained, where most of the boundaries in the sample are high-angle boundaries with misorientation angle above 15°. Annealing at 175°C for 6 h caused dislocation annihilation and slight boundary migration, leading to a quite equiaxed fine grained structure with the grain size of 2.4 μm (Fig. 1b). By the second-step annealing at high temperature, the grain size can be changed gradually in the range from sub-micrometer to several tens micrometer. These samples composed of high-angle boundaries are termed as "grained" samples, to distinguish from "subgrained" samples.

The stress-strain curves for the 50% cold-rolled and annealed samples are shown in Fig. 2a. The as-deformed 50% cold-rolled sample has a tensile strength of approximately 100 MPa, but after annealing of 175°C 24 h the strength significantly decreases, corresponding

to a decrease in the dislocation density. The strength gradually decreases by further high-temperature annealing, which is due to the slight increase in the subgrain size. It is seen that in the subgrained samples the stress-strain curves reveal a conventional continuous yielding.

The stress-strain curves for the grained samples, which have been produced by 6-cycle ARB and annealing, are shown in Fig. 2b [3]. The as-deformed 6-cycle ARB sample shows a tensile strength of 115 MPa and a relatively large total elongation. Annealing of 175°C for 6 h leads to a significant decrease in the strength, due to an increase in the grain size as well as a decrease in the dislocation density. It should be emphasized here that sharp yield point phenomena can be observed in the early stage of tensile test. After high-temperature annealing, as well as a yield point phenomena, a stress-constant region followed by work-hardening, which corresponds with the nucleation of Lüders bands and their propagation, are observed. However, when the average grain size is larger than 10 μm, yield point phenomena disappear and a conventional continuous yielding behavior is observed.

It is clearly shown from the above results that the yielding behavior of the samples strongly depends on the boundary misorientation in the fine grained region. It was also found that the yield stress is much higher in the ultrafine grained samples than in the subgrained samples at the similar grain/subgrain size range. In other words, high-angle boundaries are more effective for strengthening than low-angle boundaries.

Following hypothesis can be applied to understand the obtained results. One important criterion to reveal yield point phenomena is that samples have few mobile dislocation in an initial state. In the ultrafine grained samples, due to the difficulty in propagation of dislocation sources in the grains [7] or enhanced recovery of dislocations at high-angle boundaries, the density of dislocation sources may be quite low. Therefore, a high stress is required to activate alternative dislocation sources, e.g. at grain boundaries. On the other hand, in the subgrained samples dislocations in low-angle boundaries may act as easy dislocation sources, leading to a lower yield stress. It is therefore suggested that lack of dislocation sources is responsible for the high strength in nanostructured metals.

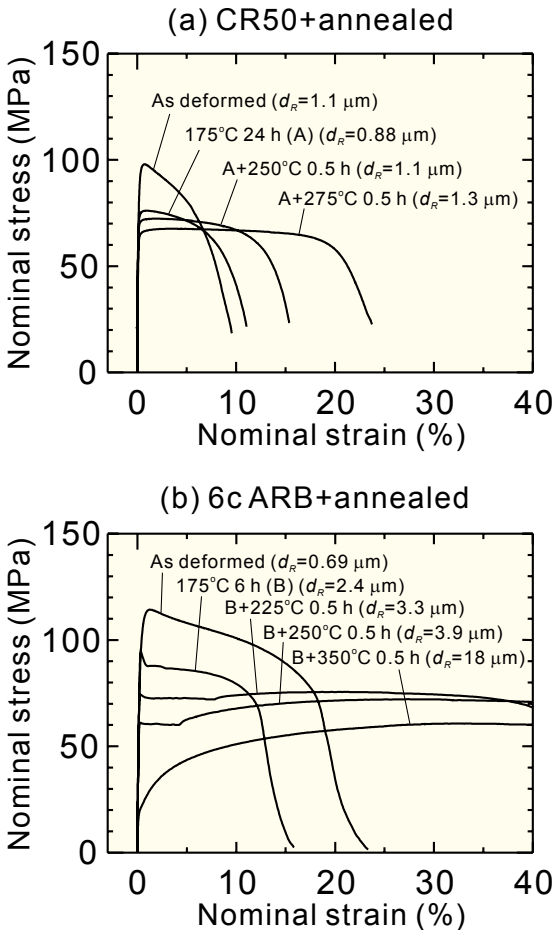

Fig. 2 Nominal stress-strain curves of the samples deformed and annealed. (a) 50% cold-rolled and annealed, (b) 6-cycle ARB processed and annealed.

References

[1] M.A.Meyers *et al.*, *Prog. Mater. Sci.* **51** (2006) 427.
[2] N.Tsuji *et al.*, *Scripta Mater.* **47** (2002) 893.
[3] N.Kamikawa *et al.*, *Acta Mater.* **57** (2009) 4198.
[4] X.Huang *et al.*, *Science* **312** (2006) 249.
[5] N.Kamikawa *et al.*, *Acta Mater.* **54** (2006) 3055.
[6] Y.Saito *et al.*, *Acta Mater.* **47** (1999) 579.
[7] T.Ohashi *et al.*, *Int. J. Plast.* **23**(2007) 897.

Keywords: nanostructure, deformation, mechanical properties
T.Furuhara, G.Miyamoto, N.Kamikawa (Microstructure Design of Structural Metallic Materials)
E-mail: kamikawa@imr.tohoku.ac.jp
URL:http://www.st-mat.imr.tohoku.ac.jp

Structural Analysis of a Variety of Approximants for Quasicrystalline Materials.

Structural analyses of o-AlPdMnSi and χ-AlPdRe approximants have been performed by single crystal X-ray diffraction. The structure of o-AlPdMnSi phase indicates a unique packing of the decagonal column with a periodicity of 0.72 nm and the pentagonal one with 0.48 nm, which are different from the typical columnar structures found in Al_3Mn and Al_3Pd. The structure of χ-AlPdRe phase indicates an i3 cluster composed of three icosahedra and a bi-capped pentagonal prism, and a pseudo Mackay cluster. The pseudo Mackay cluster consists of irregular 1st icosahedral and 2nd icosidodecahedral shells with a central heavy metal site.

After the discovery of an icosahedral quasicrystalline phase in a rapidly solidified $Al_{86}Mn_{14}$ alloy by Shechtman *et al.* in 1984 [1], a variety of researches on quasicrystals have been done in order to understand their unique physicochemical properties. For providing a realistic structure model for quasicrystals, structural information on the corresponding approximants has been frequently used. This paper demonstrates the structural features of newly found approximant phases for the decagonal Al-Pd-Mn and icosahedral Al-Pd-Re [2,3].

o-AlPdMnSi approximant [2]

The orthorhombic approximant phases such as Al_3Pd, $Al_{73.5}Pd_{22.4}Mn_{4.1}$, Al_3Mn and $Al_{75}Mn_{20}Pd_5$ indicate layered structures with 1.2 or 1.6 nm periodicity. The corresponding columnar structures in such approximants allow us to estimate atomic arrangements of the decagonal quasicrystals in the Al-Pd-Mn system. In the quaternary Al-Mn-Pd-Si system, a new orthorhombic $Al_{72}Pd_{18}Si_5Mn_5$ (here after o-AlPdMnSi; $Al_{71.7}$ $Pd_{18.5}$ $Mn_{5.0}$ $Si_{4.8}$) has been reported nearby 1/1 and 2/1- cubic AlPdMnSi approximants [4,5].

A needle-like crystal was cut out from an arc-melted alloy ingot ($Al_{69}Pd_{20}Mn_8Si_3$), and the structure was analyzed by single crystal X-ray diffraction. The structure (*Pnma*; *a*=1.4396(3), *b*=2.4003(2), *c*=7.603(2)nm) can be represented by the stacking of three types of layers (A,B,C) perpendicular to the *b*-axis. The structure of o-AlPdMnSi consists of unique stacking of the decagonal column with a periodicity of 0.72nm and pentagonal one with 0.48nm (Fig.1). This feature is different from the cases of Al_3Mn and Al_3Pd, where the structure is composed by the single column produced by stacking of the corresponding layered structures. Therefore, the unique stacking demonstrated in the o-AlPdMnSi is suggested to produce a new type of the decagonal columnar structure. The columnar structures are suggested to introduce unique periodicity in decagonal quasicrystals.

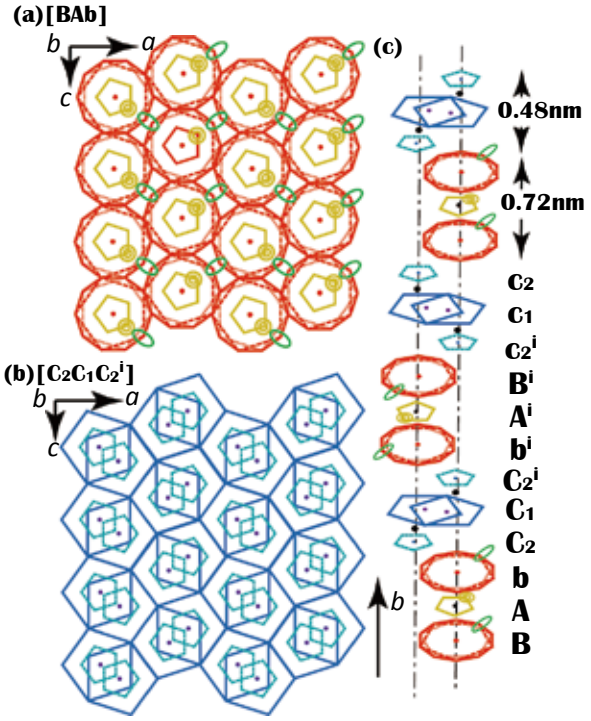

Fig. 1: (a) The tiling of layer unit [BAb] and (b) of layer unit [$C_2C_1C_2^i$]. The double circles indicate the position of Pd/Al(1) and ovals are split sites Al(24)/Pd(24). (c) The arrangement of columnar structure with the periodicity of 0.48 and 0.72 nm is shown.

χ- AlPdRe approximant [3]

In the ternary Al-Pd-Re system, a stable icosahedral i-$Al_{70}Pd_{20}Re_{10}$ and a decagonal D-$Al_{78}Pd_8Re_{14}$ have been reported.

A single crystal sample of χ-AlPdRe (*P*31c *a*=1.23744(4), *c*=2.7487(1)nm) was cut from the prepared ingot of $Al_{80}Pd_{15}Re_5$ (annealed at 750°C for 10 days).

The structure is isotypic to that of Ir_9Al_{28} [6]. The heavy metal (Pd and Re) sites of χ-AlPdRe correspond to Ir sites of Ir_9Al_{28}, suggesting the typical pseudo-decagonal motifs together with the pseudo Mackay type icosahedral cluster around a Re site.

Fig. 2 indicates sub-structure units of Pd(8)-centred icosahedra (Pd8I) and Pd(5)- centred bi-capped pentagonal prism (Pd5BPP) composed by heavy metals. Pd8I

interpenetrates with each other and produces an I-type connection [7]. Such I-type connections are further connected via a common vertex Pd(5) so as to form a decagonal columnar structure along the *a*-axis. The decagonal columns run parallel to three equivalent directions and intersect each other.

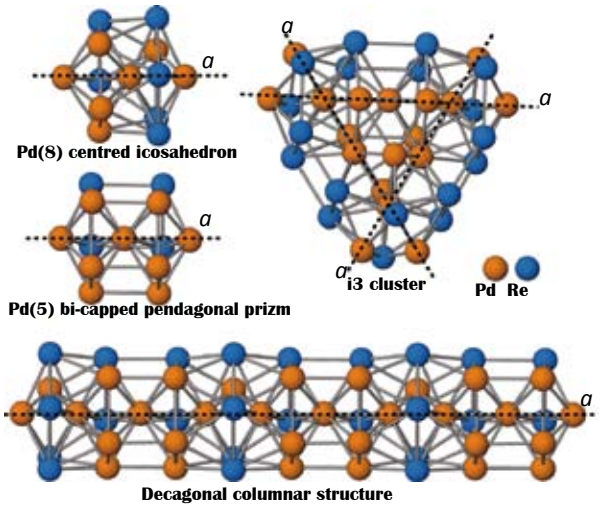

Fig.2: Pd(8)-icosahedron, Pd(5)- bi- capped pentagonal prism, pentagonal column, and i3 cluster are shown.

Fig. 3 shows the psudo-Mackay type icosahedral cluster (p-Mackay) together with its network along the *c*-axis with the Pd(5) triangle junctions. The first shell of p-Mackay is an irregular shaped polyhedron of 7 Al with Re(4) centre (i-ii). The second shell with a radius about 0.48nm (iii-iv) may be ranked into two sub-shells. One is an icosahedron produced by 12 Pd (iii) and each vertex of the Pd-icosahedron is capped by 5 Al, so as to form the Al-icosidodecahedron (iv). The second shell structure well reproduces the atomic arrangement in the typical Mackay cluster, and is similar to that observed in the structural model of i-AlPdRe.

These structural features of χ-AlPdRe are well attributed to its chemical composition nearby the center of those for i-phase and D-phase in the Al-Pd-Re system.

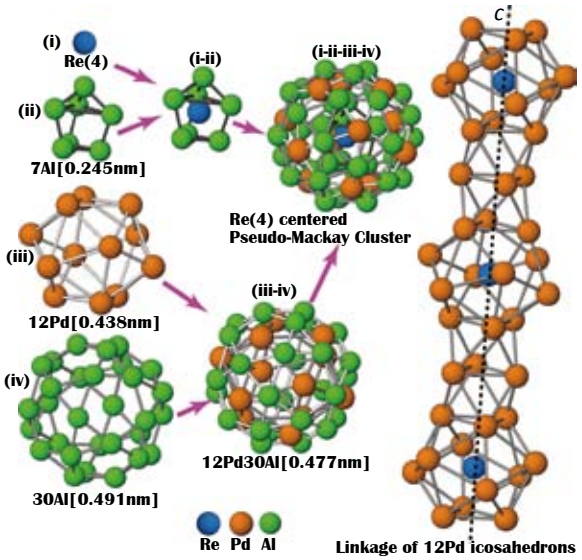

Fig.3: Re(4)-pseudo-Mackay cluster (i-ii-iii-iv) can be ranked into 4 components (i)-(iv). The values in parentheses indicate the averaged distances of the consisting atoms from the centre of the cluster. The linkage of the Pd-icosahedra along the *c*-axis is also shown.

References

[1] D. Shechtman *et al.*, *Phys. Rev. Lett.* **53** (1984) 1951.
[2] R.Simura *et al.*, *Phil. Mag.* **91** (2011) 2603.
[3] S. Suzuki *et al.*, *Phil. Mag.* **91** (2011) 2610.
[4] K.Sugiyama *et al.*, *Z. Kristalogr.* **213** (1998) 90.
[5] K.Sugiyama *et al.*, *Z. Kristalogr.* **213** (1998) 168.
[6] S.Katrych *et al.*, *J. Alloy. Compd.* **407** (2006) 132.
[7] G. Kreiner, and H.F. Franzen, *J. Alloy. Compd.* **221** (1995) 15.

Keywords: crystal structure, X-ray diffraction, quasicrystal
K.Sugiyama and R.Simura (Chemical Physics of Non-Crystalline Materials)
URL: http://www.xraylab.imr.tohoku.ac.jp/

Development of Novel Titanium Alloys with Self-adjustable Young's Modulus for Biomedical Applications

Young's modulus of metallic implant device should be sufficiently low to prevent stress shielding for the patient. However, such the Young's modulus should be sufficiently high to suppress springback for the surgeon. In order to satisfy these requirements simultaneously, we proposes a new concept, self-adjustment of Young's modulus, for biomedical titanium alloys. This concept can be achieved using deformation-induced phase transformation; the Young's modulus of only the deformed part would increase during operation, while that of the non-deformed part would remain low. In this study, the deformation-induced ω phase transformation was introduced into a β-type titanium alloy. As a result, the Young's modulus of the titanium alloy could be increased by deformation.

The stress shielding effect is one of the problems for metallic implant devices because it causes excessive bone absorption. It is believed that the Young's modulus equal to that of bone is ideal for metallic biomaterials to inhibit the stress shielding effect. Therefore, extensive efforts have been made to develop β-type titanium alloys having low Young's moduli (40–60 GPa) similar to that of bone (10–30 GPa). One such alloy developed by the authors [1], Ti-29Nb-13Ta-4.6Zr alloy (TNTZ), is a promising candidate for a next-generation metallic biomaterial, and attempts have been made to utilize this alloy in practical applications such as the production of spinal implant rods. However, when using TNTZ, some collaborating surgeons specializing in spinal diseases pointed out that the amount of springback in the spinal implant rod should be small to obtain better handling ability during operations. The amount of springback is considered to depend on both the strength and the Young's modulus of the spinal implant rod. If two spinal implant rods having the same strength and different Young's moduli are used, the spinal implant rod having a lower Young's modulus shows greater springback. The spinal implant rod made of TNTZ exhibits a low Young's modulus, resulting in greater springback. Thus, a low Young's modulus, which is one of the outstanding features of TNTZ as a metallic biomaterial and obviously a desirable property for patients, becomes an undesirable property for surgeons.

With this background, in this study, we attempted to devise a solution using metallurgical engineering to satisfy the requirements of both surgeons and patients for the Young's modulus of spinal implant rods. Fig. 1 shows the concept of self-adjustment of Young's modulus in spinal implant rod [2]. Generally, the Young's modulus of metals does not change drastically by deformation. However, for certain metastable β-type titanium alloys, non-equilibrium phases such as α', α'', and ω appear in the β matrix during deformation. If the Young's modulus of the deformation-induced phase is higher than that of the original β phase, the Young's modulus of only the deformed part of the spinal implant rod increases, but that of the non-deformed part remains low. In orthopaedic operations for treating spinal diseases, the spinal implant rod is bent by surgeons so that it corresponds to the curvature of the spine. Therefore, if a suitable titanium alloy is employed as the spinal implant rod material, springback can be suppressed by deformation-induced phase transformation occurring during bending in the course of the operation, whereas a low Young's modulus can be retained for patients.

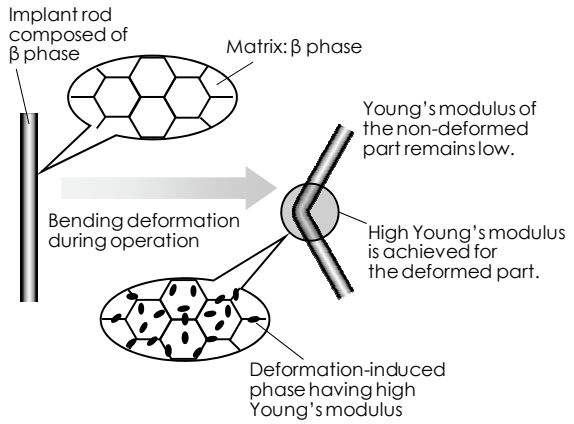

Fig.1: Concept of self-adjustment of Young's modulus in spinal implant rod.

Among the abovementioned non-equilibrium phases, ω phase is expected to increase the Young's modulus because it is well known that the presence of the ω phase, formed by aging treatment at a relatively low temperature below ~673 K, drastically increases the Young's modulus of β-type titanium alloys [3]. Further, the occurrence of the deformation-induced ω phase transformation has been reported in some β-type titanium alloys [4]. However, the effect the deformation-induced ω phase transformation on the change in the Young's modulus has never been focused. Therefore, in this study, the change in the Young's modulus of a metastable β-type titanium alloy by deformation was examined.

According to the previous report[4], Ti-12Cr alloy (Ti-12Cr) was selected as a candidate having a chemical composition in which the deformation-induced ω phase transformation is likely to occur [2]. In the results of optical microscopy, the microstructure of Ti-12Cr subjected to solution treatment (ST) comprised equiaxial grains. In contrast, after cold rolling (CR), mechanical twins were observed inside the equiaxial grains of Ti-12Cr. The electron diffraction patterns of the $[110]_\beta$ zone obtained by Transmission electron microscopy reveal that only a circular diffuse streak was observed in combination with spots derived from the β phase in Ti-12Cr-ST. However, extra spots in addition to the reflection from the β phase, considered to be derived from the ω phase, could be observed in Ti-12Cr-CR. These results confirm the occurrence of deformation-induced ω phase transformation accompanying mechanical twinning in Ti-12Cr during cold rolling.

Fig. 2 shows the results of Young's modulus measurement for Ti-12Cr-ST and Ti-12-CR [2]. In this figure, the Young's moduli of our previously developed TNTZ, which does not exhibit deformation-induced phase transformation during cold rolling [3], are also shown for comparison [2]. Ti-12Cr-ST exhibits a low Young's modulus of <70 GPa; this value is comparable to that of TNTZ-ST, which was developed as a biomedical β-type titanium alloy having a low Young's modulus. TNTZ-CR also shows a low Young's modulus that is almost equal to that of TNTZ-ST. Thus, cold rolling barely causes any change in the Young's modulus of TNTZ. However, the Young's modulus of Ti-12Cr increases by cold rolling and that of Ti-12Cr-CR exhibits > 80 GPa. After cold rolling, both alloys have different phase constitutions: no new phase formation was reported in TNTZ, but the deformation-induced ω phase was detected in Ti-12Cr. As mentioned earlier, it is well known that the ω phase drastically increases the Young's modulus of β-type titanium alloys [3]. Therefore, the increase in the Young's modulus of Ti-12Cr is considered to be derived from the deformation-induced ω phase transformation.

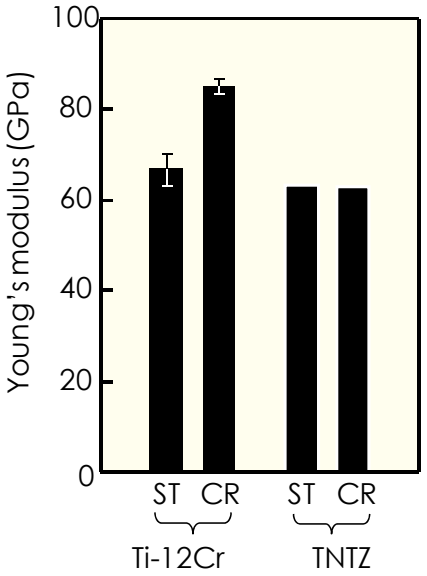

Fig. 2: Young's moduli of Ti-12Cr alloy (Ti-12Cr) and Ti-29Nb-13Ta-4.6Zr alloy (TNTZ) subjected to solution treatment (ST) and cold rolling (CR).

For spinal implant rods, the Young's modulus should be sufficiently high to suppress springback for the surgeon, but it should also be sufficiently low to prevent stress shielding for the patient. Therefore, this study proposes a novel concept—self-adjustment of Young's modulus. In order to achieve this concept, the change in Young's modulus of titanium alloys through deformation-induced phase transformation was investigated using Ti-12Cr. This alloy successfully underwent the deformation-induced ω phase transformation and then exhibited the increase in Young's modulus by deformation.

References

[1] D. Kuroda *et al., Mater. Sci. Eng. A* **243** (1998) 244.
[2] M.nakai *et al., Mater. Lett.* **65** (2011)688.
[3] T. Akahori *et al., Mater. Sci. Eng. C* **25** (2005) 248.
[4] S. Hanada *et al., J. Mater. Sci.* **21** (1986) 4131.

Keywords: alloy, biomedical, phase transformation, Young's modulus
M.Niinomi (Biomaterials Science Division)
E-mail: niinomi@imr.tohoku.ac.jp
URL: http://biomat.imr.tohoku.ac.jp/

Fabrication of Novel Cu-Ti Alloys by Aging in Hydrogen Atmosphere

Aging Cu-Ti alloys in hydrogen atmosphere significantly improves their electrical conductivity. Based on this finding, we proposed a model fabrication process of Cu-Ti alloys to improve both of their strength and conductivity. When the alloy was severely prior-deformed and then aged at a low temperature of 623 K under a high hydrogen pressure of 0.8 MPa, the tensile strength was beyond 1000 MPa and the conductivity was over 30 %IACS, The balance of the mechanical and electrical properties was comparable with that of commercial Cu-Be alloys.

Copper (Cu)-based alloys for electrical products such as lead frames and connectors are required to have high strength and good electrical conductivity. Among representative Cu alloys, Cu-Be alloys have been commercially applied because of their excellent balance of the properties [1]. However, health hazards associated with Be element have posed considerable concern, and substitutions for Cu-Be alloys are sought. As a candidate materials, age-hardenable Cu-Ti alloys containing approximately 1 to 6 at.% Ti are attractive because of their superior mechanical properties comparable to Cu-Be alloys [2]. While, the conductivity of the alloys falls somewhat below that of Cu-Be alloys. From a practical viewpoint, therefore, a way to enhance the conductivity of the alloys without degradation of the strength is much needed.

Semboshi et al. has reported that the conductivity of Cu-Ti alloys increased significantly when the alloys were aged rather in hydrogen atmosphere than conventionally in vacuum [3,4]. In the subsequent studies, the influence of aging procedure, such as hydrogen pressure, aging temperature and prior-treatment on their strength and conductivity has been investigated; aging under a high hydrogen-pressure allowed for a rapid improvement in the conductivity [5]. Aging at a low temperature provided a reasonable balance of these properties, although a long aging-time was required [6]. Cold-rolling prior to aging is useful to accelerate the improvement of both the strength and conductivity during the aging [7]. Based on these findings, in this study, we proposed a model fabrication procedure for novel Cu-Ti alloys with an excellent balance of the strength and conductivity, comparable to commercial Cu-Be alloys.

We prepared supersaturated Cu-4.2 at.% Ti specimens. They were prior-deformed at 298 K in a reduction rate of 60% and then aged at 623 K under a hydrogen pressure of 0.8 MPa. Fig. 1 shows the relationship between tensile strength and conductivity of the specimens. For comparison, that of Cu-Ti alloys conventionally aged in vacuum and commercial Cu-Be alloys are also shown [8]. The specimen exhibited a maximum strength of 1052 MPa with a conductivity of 14% IACS (%IACS: the percentage based on the conductivity of international annealed copper standard at 298 K) by the aging for 24 h in the hydrogen atmosphere. On the over-aging stage for 120 h, the specimen still had a strength of more than 1000 MPa and high conductivity of 30% IACS. The balance of the strength and conductivity was superior to that for conventional Cu-Ti alloys, and comparable with that for some commercial Cu-Be alloys. The balance of the properties must be furthermore improved by using the alloys prior-deformed more severely and aging at a lower temperature under a higher hydrogen pressure.

The microstructural evolution during prior-deformation and then aging in hydrogen atmosphere can be summarized as follows [9]; high-dense structural defects such as

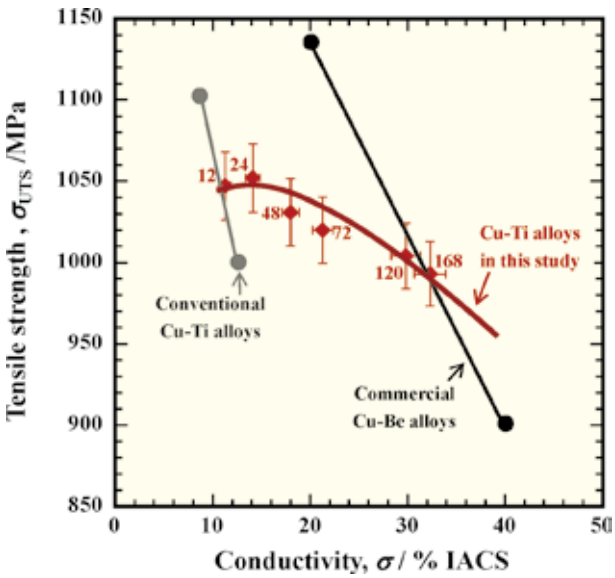

Fig. 1: Relationship between the tensile strength and electrical conductivity of Cu-4.2 at.% Ti specimens cold-rolled down to a reduction of 60% and then aged at 623 K in a hydrogen pressure of 0.8 MPa. The number beside each plot indicates the aging time in hours. For comparison, the relationships of Cu-Ti alloys conventionally aged in vacuum, and commercial Cu-Be alloys are also shown [8].

dislocations and deformation twins, with several 10 nm in width, were generated by prior-deformation in the specimens. On an early stage of aging in hydrogen atmosphere, Cu_4Ti particles dispersed finely overall the specimen, similar to the case of aging in vacuum. During the subsequent aging, the precipitation of Cu_4Ti proceeds and TiH_2 particles are spontaneously formed by the combination of diffused hydrogen with titanium in the matrix (see Fig. 2). The nucleation of Cu_4Ti and TiH_2 particles is promoted by prior-deformation, which is attributed to structural defects [7].

Strengthening of the Cu-Ti dilute alloys by aging in a hydrogen atmosphere is primarily due to the precipitation of Cu_4Ti particles, according to the Orowan mechanism [4, 10]. In addition, the improvement in conductivity is controlled by the concentration of titanium dissolved in the matrix, which is efficiently reduced by the co-formation of Cu_4Ti and TiH_2 [3]. In the specimens severely deformed and then aged at a low temperature under a high hydrogen pressure, the number density of Cu_4Ti precipitates is effectively increased, which results in efficient dispersion-strengthening. Furthermore, the nucleation of TiH_2 precipitates is accelerated in the deformed specimen, so that the conductivity is increased more rapidly during the aging. Thus, precipitation of Cu_4Ti and TiH_2 particles with a high number density and a high volume fraction is available for Cu-Ti alloys to possess an excellent balance of the strength and conductivity.

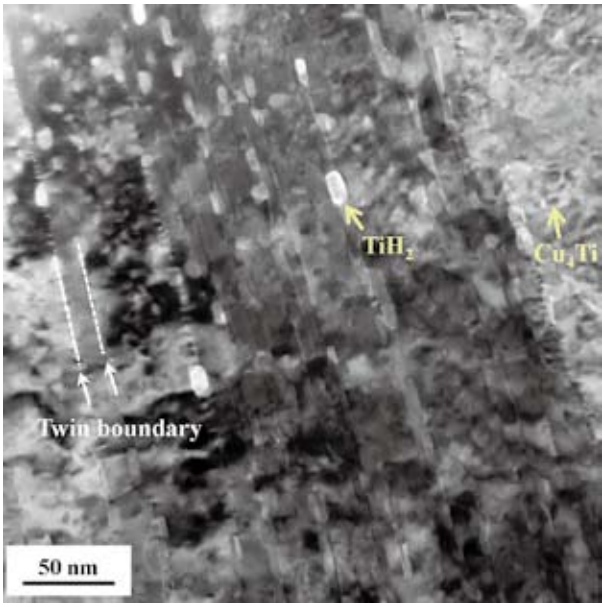

Fig. 2: Transmission electron microscopy (TEM) image of Cu-4.2 at.% Ti specimen cold-rolled to a reduction of 60%, and then aged at 653 K for 48 h in a hydrogen pressure of 0.8 MPa. Cu_4Ti particles, of several nano-meters in size, and TiH_2 particles, of approximately 10 nm, between deformation twin boundaries are found.

References

[1] P.J. Rioja and D.E Laughlin, *Acta Metall.*, **28** (1980) 1301.
[2] A. Datta and W.A. Soffa, *Acta Metall.*, **24** (1976) 987.
[3] S. Semboshi and T.J. Konno, *J. Mater. Res.*, **23** (2008) 473.
[4] S. Semboshi et al., *Mater. Sci. Eng. A*, **517** (2009) 105.
[5] S. Semboshi et al., *Mater. Trans.*, **52** (2011) 605.
[6] S. Semboshi et al., *Metall. Mater. Trans. A*, **42A** (2011) 2136.
[7] S. Semboshi et al., *Mater. Sci. Forum*, **645-646** (2010) 1315.
[8] S. Nagarjuna et al., Mater. Sci. Eng. A, **259** (1999) 34.
[9] S. Semboshi et al., *Ultramicroscopy*, **109** (2009) 593.
[10] W.E. Wang, *J. Alloys Comp.*, **238**, (1996) 6.

Keywords: mechanical properties, electrical properties, nanostructure
S. Semboshi (Hydrogen Functional Materials Division)
E-mail: semboshi@imr.tohoku.ac.jp
URL:http://www.hydrogen.imr.tohoku.ac.jp

Fracture and Hot Deformation Behavior of Co based Alloys Governed by Extremely Low Stacking Fault Energy

Cobalt based alloys have been investigated extensively to apply for medical implants and structural components used in aerospace or automobile industries. We have revealed the fracture and hot deformation behavior of Co-Cr-Mo alloys which are governed by the unique dislocation mechanisms and nature of phase stability of Co-Cr-Mo alloys. Phase-field simulation has been applied to examine the Suzuki effect observed in a Co-Ni-Cr-Mo alloy at higher temperatures. It has been established that the Suzuki effect, i.e., solute segregation to a stacking fault bounded by the Shockley partial dislocations, is essentially concomitant with high temperature deformation of Co based alloys.

Cobalt-chromium-molybdenum (Co-Cr-Mo)- based alloys have been used in various medical applications because of their excellent biocompatibility and mechanical properties. Here, we examined the fracture behavior of Co-Cr-Mo alloy consisting of γ (fcc) single phase analyzed by X-ray tomography and the deformation mode of Co-Cr-Mo alloy consisting of ε (HCP) single phase analyzed by EBSD method.

The damage process leading to fracture during tensile testing of a biomedical grade Co–29Cr–6Mo–0.14N alloy was analyzed on the basis of three-dimensional damage observation using X-ray tomography and electron backscattered diffraction of the fractured specimen (Fig.1). Initial cracking occurred at grain and annealing twin boundaries, where strain concentrates due to impingement of ε-HCP plates formed through strain-induced martensitic transformation (SIMT). Cracks propagated along the interface between the γ-FCC matrix and SIMTed ε-HCP on {1 1 1} plane, resulting in a quasi-cleavage fracture [1].

Regarding the deformation mode of Co-Cr-Mo alloy consisting of ε (HCP) single phase [2], basal <a> and prismatic <a> slips were the dominant deformation modes. The activation of these <a> slips is strongly dependent on Schmid factor, which indicates that the values of critical resolved shear stress (CRSS) for basal <a> slip and prismatic <a> slip are similar. For tensile strains up to 10%, the frequent occurrence of deformation twins could not be confirmed by EBSD analysis.

Further, the article [3] presents the dynamic recrystallization (DRX) behaviors of Co-29Cr-6Mo alloy with additions of both C and N (hereafter CCMCN alloy). The results revealed that the initial microstructure is a stable γ face-centered cubic (FCC) phase with a large number of $M_{23}C_6$ precipitates both inside the grains and at grain boundaries. The DRXed grains were observed to be uniformly distributed and to decrease with strain (Fig.2). The high volume fraction of Σ3 boundaries was observed after the DRX, indicating a close relation between the DRX mechanism and Σ3 boundary formations. In addition, the activation energy Q of CCMCN alloy was observed to be higher as compared to those of alloys without C or N addition and that with N addition.

As demonstrated above, the mechanical properties of Co-based alloys are closely related to the stability of HCP-structure and FCC-structure. Besides the above mentioned detrimental aspect, the SIMTed ε-HCP in Co-Cr-Mo alloys has beneficial aspects as well. It can enhance Young's modulus, and improve strength and wear resistance [4]. Co-Ni-based superalloys with relatively high FCC-phase stability exhibit high ductility by dislocation slip

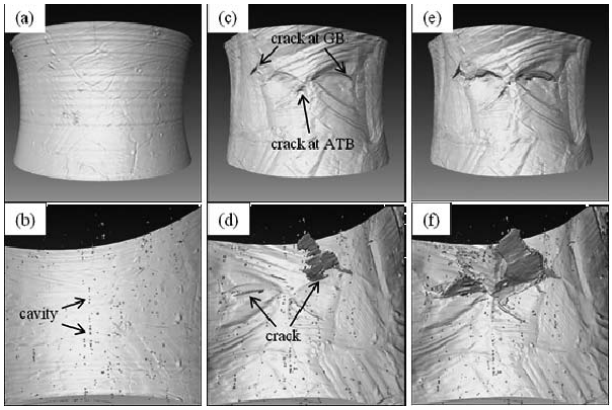

Fig.1 3D tomographic reconstruction of Co-29Cr-6Mo-0.14N alloy at three different relevant damage steps: (a), (b) initial state; (c), (d) crack initiation state and (e), (f) the state just before fracture. Fig. 1 (a), (c), (e) and (b), (d), (f) indicate the outer surface and the inner cracks inside the specimen, respectively.

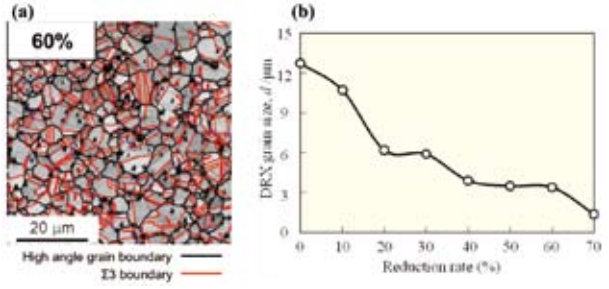

Fig. 2 (a) Microstructure of deformed sample at 1423 K at 1 s^{-1} at reduction rate of 60%. (b) Mean grain size as a function of reduction rate.

[5]. The stability of HCP phase affects the nature of stacking faults which governs the plastic behaviors by both dislocation slip and twinning.

The phase-stability at stacking fault can be significantly affected by segregation of solute atoms, i.e. Suzuki segregation. To date, Suzuki segregation in Co-alloys has never been verified experimentally despite many attempts by researchers all over the world. Atomistic simulations are commonly applied to studies of interfacial segregation, but it is quite difficult to apply atomistic calculation to multinary systems such as as cobalt-alloys.

Phase-field method is a simulation method based on thermodynamics and diffuse interface model, which is applicable to microstructural evolution and interfacial reaction in nanometer and micrometer length scale. It has been developed as powerful tool to bridge the gap between the atomistic and macroscopic simulations. In the present study, we have developed a phase-field model of segregation in order to examine the Suzuki-segregation in Co alloys (Fig.3).

Fig.4 shows the distributions of alloying elements at and around a stacking fault in Co-30Ni-20Cr-10Mo (wt%) alloy (hereafter, denoted as CNCM-alloy) equilibrated at 973 K in a simulation where elastic strain energy is taken into account [6]. Ni and Nb were strongly depleted and Cr segregated at the stacking fault, while Mo exhibits neither segregation nor depletion. In a simulation in which elastic strain energy is neglected, Mo segregation was observed, implying that the chemical interaction for segregation and the size effect is compensating each other. The stacking fault energy dramatically decreased from 35 mJ/m^2 to -937 mJ/m^2, as a result of the segregation. This agree with the experimentally observed spontaneous formation of very wide stacking faults in the deformed and subsequently annealed CNCM-alloy (Fig. 5).

Thus, the segregation at stacking fault in Co-alloy has been computationally verified for the first time. This approach can be applied to the alloy designing for further improvements of biomedical and industrial Co-alloys.

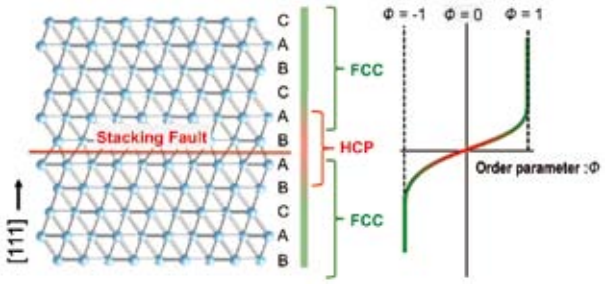

Fig.3 Model of stacking fault used for the calculation.

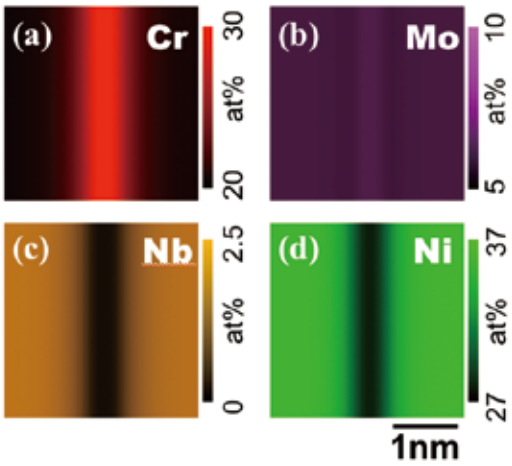

Fig.4 Distributions of (a) Cr, (b) Mo, (c) Nb and (d) Ni at and around a stacking fault in Co-30Ni-20Cr-10Mo (wt%) alloy equilibrated at 973 K.

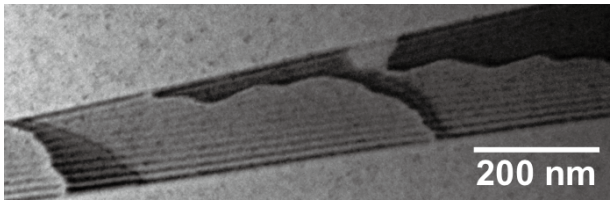

Fig.5 TEM image of stacking fault in Co–Ni-based superalloy single crystal compressed to 2 % and subsequently annealed at 973 K for 3.6 ks.

References

[1] S. Kurosu , H. Matsumoto, A. Chiba, C. Landron, D. Fabregue and E. Maire: *Scripta Materialia*, **64** (2010) 367-370.

[2] H. Matsumoto, S. Kurosu, B.S. Lee, Y. Li, A. Chiba: *Scripta Materialia*, **63** (2010) 1092-1095.

[3] Y. Yamashita, Y. Li, E. Onodera, H. Matsumoto and A. Chiba, Mater.Trans. **51** (2010) 1633-1639.

[4] A. Chiba, K. Kumagai, N. Nomura, S. Miyakawa . Acta Materialia **55** (2007) 1309-1318.

[5]A. Chiba X. G. Li and M. S. Kim, *Philosophical Magazine A* **79** (1999) 1533-1544.

[6] Y. Koizumi, S. Suzuki, T. Otomo, S. Kurosu, Y.P Li, H. Matsumoto and A. Chiba, Supplemental Proceedings: vol.2 Materials Fabrication, Properties, Characterization and Modeling, TMS 2011, pp.409-416.

Keywords: Co-Cr-Mo alloy, fracture behavior, Suzuki effect.
A. Chiba, Y. Koizumi, H. Matsumoto, and Y. Li (Deformation Processing).
E-mail: a.chiba@imr.tohoku.ac.jp.
URL: http://www.chibalab.imr.tohoku.ac.jp/english/index.php

Excitation Mechanism of Silver Ionic Lines through Collisions with Metastable Atoms of Plasma Gas in Glow Discharge Plasmas.

Emission spectra of silver from glow discharge plasmas using argon, krypton, and a krypton-argon gas mixture were analyzed to elucidate the excitation phenomenon of silver ionic lines occurring in collisions with the plasma gases. The intensities of the ionic lines which were assigned to the $4d^9 5p$ - $4d^9 5s$ transition were largely different between argon and krypton; for instance, the intensity of the Ag II 243.78-nm line emitted form the krypton plasma was 5 times larger than that from the argon plasma, while the Ag 228.00-nm line yielded much larger intensity in the argon plasma by a factor of 70. This effect can be explained by an excitation process through collisional energy transfer from the metastable atom of argon or krypton to a silver ion in the ground state (Penning excitation). This type of collision requires both matching in the excitation energy between the colliding partners and conservation in the total spin before and after the collision. The $3p^5 4s$ metastable of argon (11.72 eV and 11.55 eV) and the $4p^5 5s$ metastable of krypton (10.56 eV and 9.92 eV) would take part in the collision, and principally determine the population of the $4d^9 5p$ excited levels of the silver ion.

Glow discharge optical emission spectrometry (GD-OES) is extensively employed for the direct analysis of solid samples, because the GD source has several benefits such as rapid sampling through cathode sputtering, minimal sample pretreatment, and a wide concentration range in the quantification. Ionization /excitation phenomena occurring in the plasma should be investigated to determine the analytical line as well as the optimum discharge conditions in GD-OES. Previous studies have reported that intense emission lines of the singly-ionized atom are observed in several elements, such as copper [1, 2], nickel [3], cobalt [4], and iron [5], of which spectrum patterns are largely varied by the kind of the plasma gas employed. As similar to all other plasma sources operating at low pressures, the difference is not only in their relative intensities but in the kind of emission lines that can be excited for each plasma source [6]. This effect promoted the studies on the excitation process in GD-OES.

Several papers indicated that the excitation of ionic lines could be caused through a charge transfer collision in the GD plasma [7]. This type of collision is generally represented by the following equation: $M^g + Ar^+ \rightarrow M^{+*} + Ar^g + \Delta E$, where the superscripts ^{g}, $^+$, and * represent a ground state, an ionic state, and an excited state, respectively, and ΔE means the energy difference before and after the collision. However, it is considered that the excited levels belonging to the $4d^9 5p$ electron configuration of silver ion (the $4d^9 5p$ excited levels) would be little populated through the charge transfer collision with the argon ion because the total excitation energy of the $4d^9 5p$ levels is fairly larger than the internal energy of the argon ion, whereas the emission lines assigned to the $4d^9 5p$-$4d^9 5s$ transition can be clearly observed in the argon GD plasma [8]. Therefore, any different process should be taken into account for this excitation. Our study suggests an excitation mechanism in which a metastable atom of the plasma gas is involved, represented by the following equation: $Ag^{+g} + Ar^m \rightarrow Ag^{+*} + Ar^g + \Delta E$, where the superscript ^{m} represents a metastable state [9]. This mechanism well explains the difference in the emission intensities of the silver ionic lines between in an argon plasma and in a krypton plasma.

Excitation mechanism of Ag ionic lines [9]

Fig. 1 shows a detailed energy level diagram regarding the $4d^9 5p$ excited state of singly-ionized silver when silver ions in the ground state are in the plasma with atomic species of argon or krypton. One can find several correspondences in the excitation energy between the $4d^9 5p$ excited levels and the metastables of argon, $3p^5 4s$ $[3/2]_2$ (11.55 eV) and $3p^5 4s$ $[1/2]_0$ (11.72 eV) [10], and of krypton, $4p^5 5s$ $[3/2]_2$ (9.92 eV) and $4p^5 5s$ $[1/2]_0$ (10.56 eV) [11]. It is thus suggested that an excitation mechanism in which a metastable atom of the plasma gas is involved, represented by the following equation: $Ag^{+g} + Ar^m$ (or Kr^m) $\rightarrow Ag^{+*} + Ar^g$ (or Kr^g) $+ \Delta E$. This mechanism, so-called Penning excitation, well explains the difference in the emission intensities of the silver ionic lines between in an argon plasma and in a krypton plasma.

Fig. 2 shows a plot of the ratio of the intensity in a pure argon plasma to that in a pure krypton plasma for 6 Ag I lines and 27 Ag II lines against the sum of the first ionization potential and the excitation energy (total excitation energy). The intensity ratios of the Ag I lines are 1.08 - 1.20. Their intensities emitted from the argon plasma are slightly larger than those from the krypton plasma but they are not so different, thus indicating that the sampling amounts are similar between these plasmas. On the other

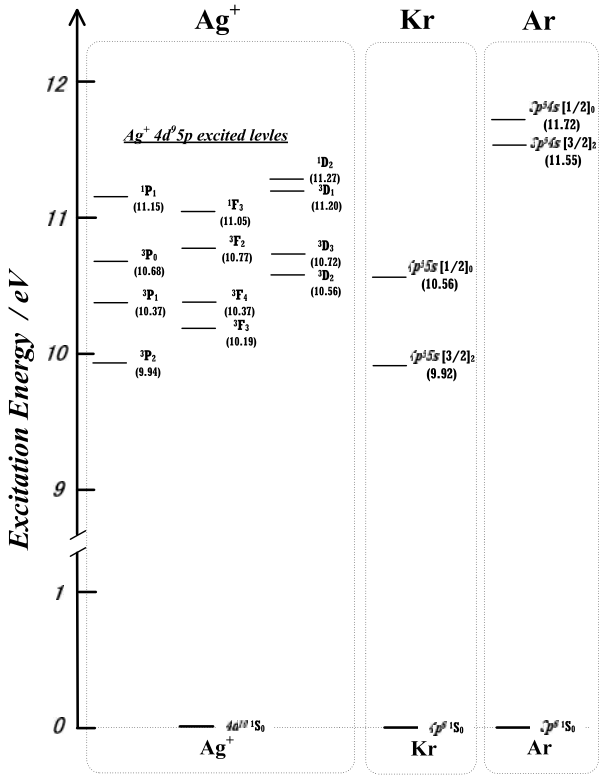

Fig. 1 Correlation of the energy level diagram between the 4d^{9}5p excited levels of silver ion and the metastable levels of argon and krypton. After Ref. [9].

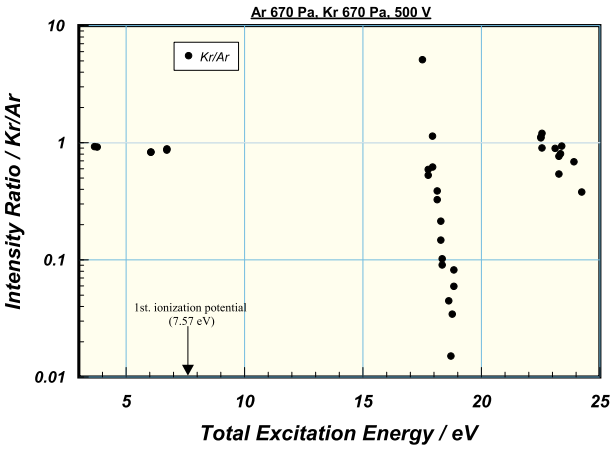

Fig. 2 Ratios of the emission intensity observed in an argon plasma to that in a krypton plasma for silver emission lines as function of their total excitation energies. Sample: pure silver; plasma gas pressure: 670-Pa Ar / 670-Pa Kr; discharge voltage: 500 V (fixed). After Ref. [9].

hand, the intensity ratios of the Ag II lines assigned to the 4d^{9}5p-4d^{9}5s transition differ greatly depending on the excitation energy. In the Ag II 243.78-nm line (from the 4d^{9}5p ^{3}**P**$_2$ level, 17.52 eV), the intensity from the argon plasma is 5 times smaller than that from the krypton plasma; however, the emission intensities from the krypton plasma become drastically reduced with increasing the excitation energy whereas those from the argon plasma become elevated, resulting in the intensity ratios of more than 10 at total excitation energies of 18.5 - 18.9 eV. Singlet Ag II lines, such as the Ag II 222.96 nm (from the 4d^{9}5p ^{1}**D**$_2$ level, 18.85 eV) and the Ag II 228.00 nm (from the 4d^{9}5p ^{1}**P**$_1$ level, 18.71 eV), have much larger emission intensities in the argon plasma than in the krypton plasma.

A particular 4d^{9}5p level of the silver ion is selectively excited in the krypton plasma, whereas all of the 4d^{9}5p levels can be populated in the argon plasma. A correspondence in the excitation energy between the 4d^{9}5p excited levels of the silver ion and the argon or the krypton metastables is the most important factor for determining the spectrum pattern from these glow discharge plasmas.

References

[1]E.B.M. Steers and R.J. Fielding, J. Anal. Atom. Spectrom., 2 (1987) 239-244.
[2]K. Wagatsuma and K. Hirokawa, Spectrochim. Acta Part B, 46 (1991) 269-281.
[3]K. Wagatsuma and H. Honda, Spectrochim. Acta Part B, 60 (2005) 1538-1544.
[4]K. Wagatsuma, Anal. Bioanal. Chem., 393 (2009) 2067-2074.
[5]K. Wagatsuma and K. Hirokawa, Spectrochim. Acta Part B, 51 (1996) 349-374.
[6]K. Wagatsuma and K. Hirokawa, Anal. Chem., 57 (1985) 2901-2907.
[7]O.S. Duffendach and J.G. Black, Phys. Rev., 34 (1929) 35-43.
[8]K. Wagatsuma, Z. Phys., D37 (1996) 231-239.
[9]K. Wagatsuma, Spectrosc. Lett., 44 (2011) 151-157.
[10]C.E. Moore, Atomic Energy Levels Vol. I, NBS Circular 467, Washington DC, (1948).
[11]C.E. Moore, Atomic Energy Levels Vol. II, NBS Circular 467, Washington DC, (1952).

Keywords: atomic emission spectrometry, glow discharge plasma, Penning excitation
K.Wagatsuma, S. Sato and S. Kashiwakura (Analytical Science)
E-mail: wagatuma@imr.tohoku.ac.jp
URL:http://wagatsuma.imr.tohoku.ac.jp

Synthesis, Boron Nonstoichiometry and Properties of Perovskite-type $ErRh_3B_x$ Ternary Borides

Polycrystalline of $ErRh_3B_x$ is synthesized by the arc-melting method. The $ErRh_3B_x$ compounds have a perovskite-type cubic structure (space group: $Pm\bar{3}m$). The solid solution range of perovskite-type phase exists for the boron concentration from x = 1.000 to 0.610. The lattice parameter *a* depends on x, and varies linearly from *a* = 0.4151 nm (x = 1.000) to 0.4063 nm (x = 0.610). The micro-Vickers hardness of the $ErRh_3B_x$ increases with increasing their B content. The hardness of stoichiometric $ErRh_3B_{1.000}$ is 8.6 ± 0.3 GPa. The thermo-gravimetric curve indicates that the onset-temperature of oxidation of $ErRh_3B_{1.000}$ is 1303 K. The weight gain of $ErRh_3B_{1.000}$ during heating in air to 1473 K is 0.7 %.

Many studies of simple and complex perovskite and Cu_3Au-type oxides have been performed due to the interesting features of superconductor, insulator-metallic transition, ion conduction characteristics, dielectric properties, and ferroelasticity [1-3]. On the other hand, there have been few studies on non-oxide perovskite and Cu_3Au-type compounds such as $RERh_3B_x$ (*RE*: rare earth metal), where RE and, Rh and B atoms are positioned at vertices, the face-centered sites and the body-centered site of the cubic, respectively, as illustrated in Fig. 1.

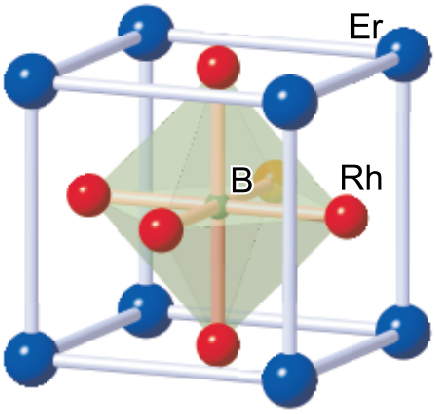

Fig. 1 Schematic representation of crystal structure of $ErRh_3B_x$.

In the present study [4], we introduce the successful synthesis of the perovskite-type $ErRh_3B_x$ ternary borides by an arc-melting method. The solid solution range of boron in the $ErRh_3B_x$ is clarified by X-ray diffraction (XRD) analysis, and the change of the lattice constant of the compounds is investigated as a function of the boron concentration x. Micro-Vickers hardness and thermochemical properties are studied for $ErRh_3B_x$ in order to investigate features of the bond.

The compound corresponded to the atomic ratio Er:Rh:B = 1:3:1; stoichiometric $ErRh_3B$ exists at the rhodium-rich portion of the Er-Rh-B tentative ternary phase diagram as shown in Fig. 2. Ternary compounds $ErRh_3B_2$ (monoclinic system, space group: *C*2/*m*) and $ErRh_4B_4$ (tetragonal system, space group: $P4_2/nmc$) also exist close to $ErRh_3B$. $ErRh_3B$, $ErRh_3B_2$ and $ErRh_4B_4$ are paramagnetic, ferromagnetic and reentrant-type superconducting compounds, respectively [5].

All the synthesized samples had a silvery metallic luster. According to chemical analyses using ICP method, the chemical compositions of the obtained samples almost corresponded to the atomic ratio of the starting compositions.

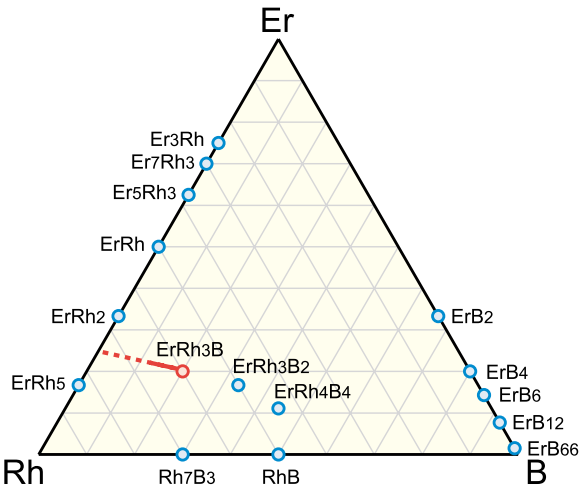

Fig. 2 Tentative phase diagram in the Er-Rh-B system. Red line indicates $ErRh_3B_x$ compounds.

By varying x in $ErRh_3B_x$, the nonstoichiometry of boron is investigated. In the cases of boron content x = 0.444 and 0.210, the second phase coexisted. Fig. 3(a) shows the variation of the lattice constant *a* as a function of boron concentration x in the cubic system of $ErRh_3B_x$. The lattice expansion with increasing boron concentration x in the compound supports the solid solution range of boron in $ErRh_3B_x$. That is, it was found that the nonstoichiometric phase exists for the boron concentration from x = 1.000 to 0.610. All compounds $ErRh_3B_x$ have a perovskite-type cubic structure (space group: $Pm\bar{3}m$). On the other hand, the solid solution range for Sc and Ce-systems exist for the boron concentration from x = 1.000 to 0.000.

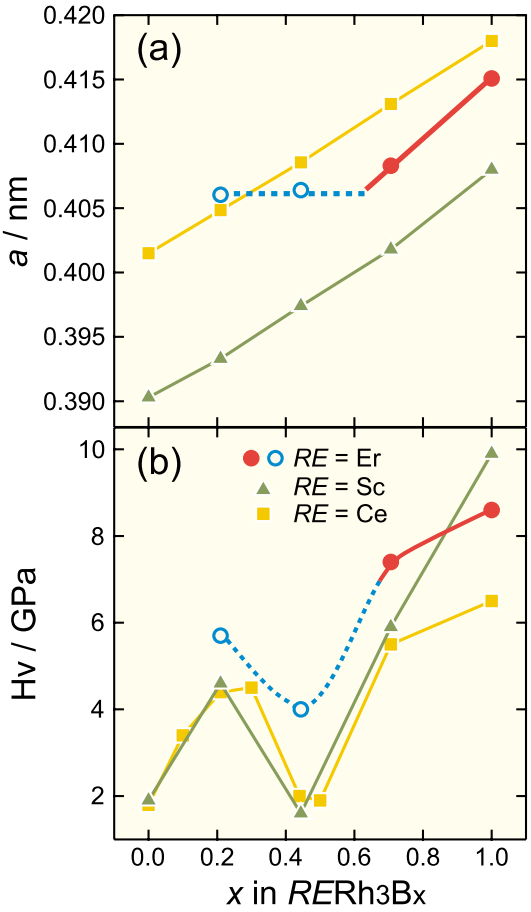

Fig. 3 (a) Lattice constant *a* and (b) micro-Vickers hardness of $ErRh_3B_x$ as a function of boron content. Open blue circles represent existence of second phase.

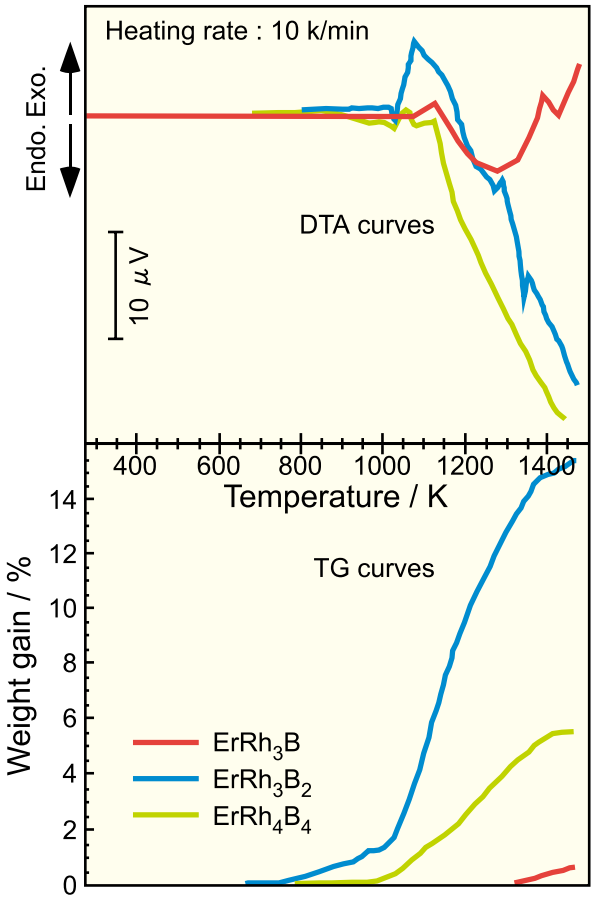

Fig. 4 TG-DTA curves for stoichiometric $ErRh_3B$. Samples are heated in air up to 1473 K at 10 K/min. Data for $ErRh_3B_2$ and $ErRh_4B_4$ are given as references.

Fig. 3(b) shows the relationship between B concentration x and micro-Vickers hardness Hv for $ErRh_3B_x$. The value of Hv is distributed over 4.0∼8.6 GPa. Similar to boron nonstoichiometry $ScRh_3B_x$ [6,7] and $CeRh_3B_x$ [8,9] compounds, the anomalous drop of hardness around x =0.5 was noted.

On the basis of TG-DTA between room temperature and 1473 K, it was found that the oxidation of the stoichiometric compound $ErRh_3B$ starts at 1303 K and the final weight gain is 0.7%. The perovskite-type $ErRh_3B$ has very high resistance for oxidation compare to layer-structure compound $ErRh_3B_2$ and cluster-including compound $ErRh_4B_4$ (Fig. 4).

The solid solution range of boron in $ErRh_3B_x$ is clarified as $0.610 \leqq x \leqq 1.000$. The micro-Vickers hardness for $ErRh_3B_x$ varies with x similar to those of Sc and Ce-systems. Oxidation of $ErRh_3B$ starts at 1303 K and the final weight gain is 0.7% (room temperature to 1473 K).

References

[1] F. Galasso, *Perovskites and High-Tc Superconductors*, Gordon and Breach, London, 1990.
[2] H. Iwahara, M. Balkanski, T. Takahashi and H. L. Tuller (eds.), *Solid State Ionics*, Elsevier, Amsterdam, 1992.
[3] P. Rogl and L. Delong, J. Less-Common Met. **91** (1983) 97.
[4] T. Shishido *et al.*, *Pacific Sci. Rev.* **12** (2011) 254.
[5] T. Shishido *et al.*, *J. Solid State Chem.* **133** (1997) 82.
[6] T. Shishido *et al.*, *J. Alloys Compd.* **309** (2000) 107.
[7] K. Yubuta *et al.*, *J. Alloys Compd.* **471** (2009) 341.
[8] T. Shishido *et al.*, *J. Alloys Compd.* **426** (2006) 304.
[9] K. Yubuta *et al.*, *J. Alloys Compd.* **426** (2006) 308.

Keywords: ternary boride, crystal structure, hardness, oxidation resistance
K. Yubuta and T. Shishido
(Research Center of Crystal Growth, Advanced Research Center of Metallic Glasses)
E-mail: yubuta@imr.tohoku.ac.jp
URL:http://www.arcmg.imr.tohoku.ac.jp

Magnetic Field Effect for the Decomposition Temperatures of MnBi

Differential thermal analysis were carried out for MnBi in fields up to 45 T. Decomposition temperatures Tt (MnBi→$Mn_{1.08}Bi$ + liquid Bi) and Tm ($Mn_{1.08}Bi$→Mn + liquid Bi) rise 84 K and 4 K by applying 45 T, respectively. Consequently, the equilibrium state of MnBi can be controlled by magnetic fields

Ferromagnetic compound MnBi exhibits unique magnetic and structural properties. With increasing temperature from room temperature, MnBi undergoes the first order magnetic phase transition from the ferromagnetic to the paramagnetic state at T_t ~630 K, accompanied by a decomposition from MnBi to $Mn_{1.08}Bi$ and liquid Bi. On the bases of high field differential thermal analysis (DTA) experiments for MnBi, Koyama *et al.* reported that T_t increases at the rate of 2 K/T in fields up to 14 T [1]. In order to study the effect of magnetic fields on the phase transitions, DTA experiments under high magnetic fields is one of the most important experiments. In addition, it requires high magnetic fields to investigate the potential of materials at the early stage of the development. However, there is no instrument for thermal analysis under high magnetic fields over 20 T in the world.

In this work, for investigating the effects of high magnetic fields for the decomposition process of MnBi, high field DTA experiments for MnBi were carried out in fields up to 45 T using the hybrid magnets with 32 mm room temperature bore by combining a new developed DTA instrument at HFLSM (IMR, Tohoku Univ.) and NHMFL (Florida State Univ.).

Fig.1 shows the DTA probe with 32 mm in diameter for DTA experiments using the hybrid magnets. Two Pt-PtRh type thermocouples were inserted into the quartz tube with 14 mm in diameter. The sample (MnBi powder) and reference sample (Al_2O_3 powder) were wrapped in aluminum film and attached to the tip of the thermocouples. The samples were heated by the nichrome heater inside the water cooling jacket. The DTA data were obtained in fields up to 45 T and in the temperature range from 300 K to 773 K during the heating at a rate of 6-7 K/min.

Fig.2 (a) and (b) shows the DTA curves of MnBi, which are measured at the HFLSM (a) and the NHMFL (b)[2]. Although the vibration noises of the water-cooled coils in the hybrid magnet were detected, the endothermic peaks due to the decompositions were clearly observed even in 45 T. As shown in this figure, T_t shifts to a higher temperature. Furthermore T_m ($Mn_{1.08}Bi$→Mn + liquid Bi) slightly shifts to a higher temperature by applying high magnetic fields. Fig.3 shows the magnetic fields dependence

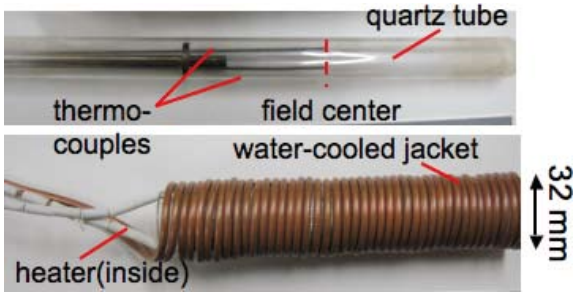

Fig.1 High field DTA probe with 32 mm in diameter.

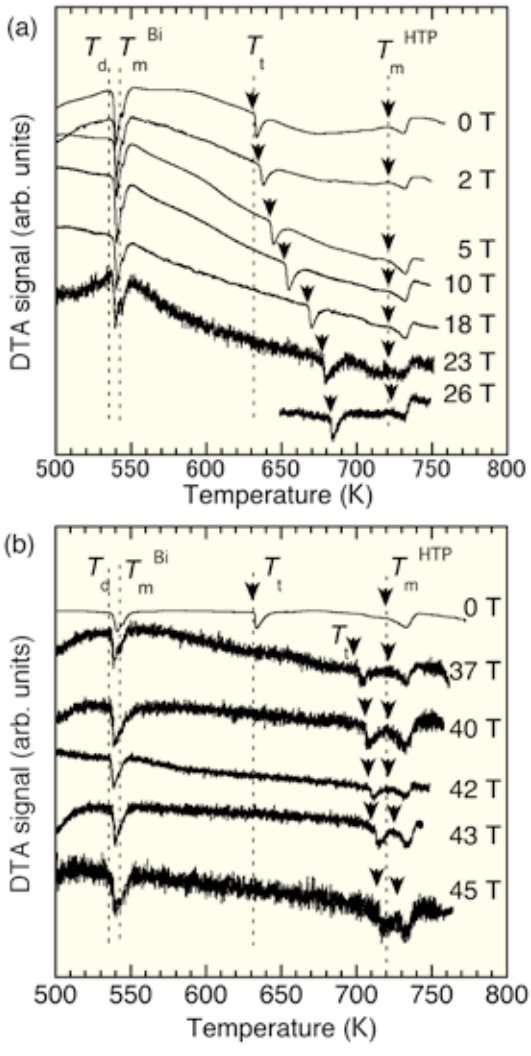

Fig.2 DTA curves for MnBi in various magnetic fields up to 45T, which are measured at the HFLSM, Japan (a) and the NHMFL, USA (b).

of the transformation temperatures T_t and T_m of the Mn-Bi compound in fields up to 45 T. The decomposition temperature T_t increases almost linearly with increasing B up to ~20 T at a rate of ~2 K/T, as shown by the broken line in Fig. 3. However, we can see that the data over ~20 T deviate from the broken line (~2 K/T) and T_t reaches very close to T_m at B = 45 T. In addition, the peritectic temperature T_m increases with increasing B, which is clearly observed over 40 T.

Fig.4 shows the typical results for the magnetic field dependence of the sample temperature in the vicinity of 689 K. In this measurement, the sample was heated to 689.5 K in B = 11.5 T. In this condition, the sample contains paramagnetic $Mn_{1.08}Bi$ and liquid phase. After that, the magnetic field was generated from 11.5 T to 45 T. As shown in this figure, we observed exothermic and endothermic peaks. In other words, this is a magnetocaloric effect. Considering the phase diagram (fig.3), exothermic and endothermic peaks are due to the phase transitions from paramagnetic $Mn_{1.08}Bi$ and liquid phase to field induced ferromagnetic MnBi for increasing B and from field induced ferromagnetic MnBi to paramagnetic $Mn_{1.08}Bi$ and liquid phase, respectively. This is, the field induced composition and decomposition process occur in the Mn-Bi system.

The high field DTA measurements in fields up to 45 T shows that not only the T_t but also T_m increased by magnetic fields. Furthermore, we observed magnetpcaloric effect in 11.5-45 T in the vicinity of 689 K. Consequently, the composition, decomposition temperatures and equilibrium state of MnBi can be controlled by high magnetic fields.

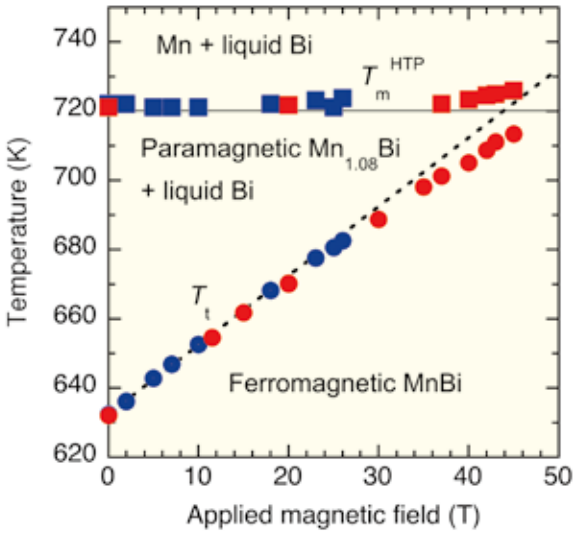

Fig. 3 Magnetic fields dependence of T_t and T_m. Blue points and red points indicate the data taken at HFLSM and NHFML, respectively.

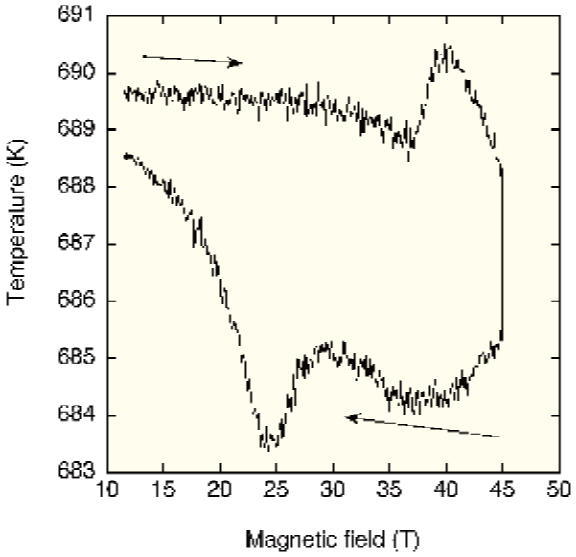

Fig.4 Magnetic field dependence of sample temperature in the vicinity of 689 K.

References

[1] K. Koyama, T. Onogi, Y. Mitsui, Y. Nakamori, S. Orimo, and K. Watanabe, Mater. Trans. 48, 2414-2418(2007).

[2] K Koyama, Y. Mitsui, E. S. Choi, Y. Ikehara, E. Palm, and K. Watanabe, J. Alloy. Compd. 509, L78-80 (2011)

Keywords: Differential thermal analysis, phase transitions, high magnetic fields

Y. Mitsui[1], K. Koyama[2], E. S. Choi[3], Y. Ikehara[1], E. Palm[3], and K. Watanabe[1]

1)HFLSM, IMR, Tohoku Univerisity 2) Graduate school of science and technology, Kagoshima Univ. 3)NHMFL, Florida State Univ.

E-mail: mitsui@imr.tohoku.ac.jp